Australasian Physical & Engineering Sciences in Medicine (2019) 42:1117–1128
https://doi.org/10.1007/s13246-019-00811-z

SCIENTIFIC PAPER

Ordered subsets Non-Local means constrained reconstruction for sparse view cone beam CT system

Yining Hu[1,2,5] · Zheng Wang[1] · Lizhe Xie[3,4] · Limin Luo[1,2,5]

Received: 4 March 2019 / Accepted: 17 October 2019 / Published online: 9 December 2019

Abstract

Sparse-view sampling scans reduce the patient's radiation dose by reducing the total exposure duration. CT reconstructions under such scan mode are often accompanied by severe artifacts due to the high ill-posedness of the problem. In this paper, we use a Non-Local means kernel as a regularization constraint to reconstruct image volumes from sparse-angle sampled cone-beam CT scans. To overcome the huge computational cost of the 3D reconstruction, we propose a sequential update scheme relying on ordered subsets in the image domain. It is shown through experiments on simulated and real data and comparisons with other methods that the proposed approach is robust enough to deal with the number of views reduced up to 1/10. When coupled with a CUDA parallel computing technique, the computation speed of the iterative reconstruction is greatly improved.

Keywords Image reconstruction · Tomography · Cone beam CT · Sparse view · Low dose

Introduction

Radiation exposure has become one of the major concerns in CT scans [1–3]. Dose reduction by optimizing hardware settings have been discussed in [4, 5]. However, lowering the radiation dose via reducing either tube current or tube voltage will result in degraded projections. Another option is to reduce the number of projection angles. This approach has been used in dental implant applications [6, 7]. A significant benefit of reducing the number of projection angles is that the signal-to-noise ratio of each projected image can be maintained, while the exposure time is reduced. However, the lack of angular sampling leads to severe spurious artifacts when using analytical reconstructions. Although iterative reconstruction algorithms can alleviate the scattering artifacts to a certain extent, fewer observations increase the ill-posedness of the reconstruction problem and accordingly the probability to fall into local extrema.

In recent years, compressed sensing (CS) theory has provided an efficient way of solving inverse problems with sparse measurements [8]. It has been widely applied to medical image reconstruction since Sildky and Pan introduced the Total-Variation minimization for 3D sparse view CT reconstruction in 2008 [9]. Lugstig [10] and Trazasko [11] have proposed CS methods for Magnetic Resonance Imaging reconstruction from sparse sampling. CS was also introduced in bioluminescence and optical coherence tomography in [12, 13]. The CS frames have been proven more effective than previous methods in sparse scans [14, 15]. The TV minimization model, equivalent to L1 minimization, was considered in sparse view reconstructions in [15, 16]. A TV-stoke method was reported by Liu to improve the TV model [17]. The TV model is proven to obtain stable reconstructions for piecewise constant regions of interest (ROIs) [18]. The TV reconstruction model in sparse view CT systems have been intensively investigated Sidky and Pan's group in

✉ Lizhe Xie
xielizhe@njmu.edu.cn

1 School of Cyber Science and Engineering, Southeast University, Nanjing, China

2 Key Laboratory of Computer Network and Information Integration (Southeast University), Ministry of Education, Nanjing, China

3 Institute of Stomatology, Nanjing Medical University, Nanjing, China

4 Jiangsu Key Laboratory of Oral Diseases, Nanjing Medical University, Nanjing, China

5 Centre de Recherche en Information Biomédicale, Sino-Francais (LIA CRIBs), Rennes, France

[19–21]. Sidky et al. proposed a non-convex version of TV constrained for high sparseness scans [22]. The anisotropic TV minimization has been also applied to limited-angle CT reconstruction [23]. Chen has extended the theory and proposed PICCS methods for cardiac CT reconstruction from highly under-sampled projections [24, 25].

Besides TV-model, the L0 minimization model is also frequently applied in sparse view reconstructions. Candes et al. pointed out that, with very sparse measurements, the semi-L0 norm can provide smoother signal recovery [26]. The L0-norm based regularizations have been applied for sparse view CT reconstructions in [27, 28]. The L0 norm based model is non-convex, therefore the optimization is more arduous than for the TV based model. We introduced an optimization scheme to approximate the L0 norm constraint in [29], and we used a modified Gamma prior to build a monotonically decreased cost function [30, 31]. Both of these methods lead to better reconstructions than TV model in sparse view condition.

Although both TV and L0 norm based model can be exploited to sparse view CT reconstruction and have been shown efficient, there are still some drawbacks that cannot be ignored. The TV based model may lead to degraded results as the number of views decreases; the L0 norm based model, although having very good performance in phantom study, may require a time consuming optimization when dealing with real acquisitions due to the increased complexity of the scanned object.

The Non-Local means (NLM) filter, shown particularly efficient in image denoising [32–34], has also been introduced to tomography reconstruction as a robust regularization technique [35, 36]. Li proposed a prior-image induced hybrid nonlocal means that makes use of a high-dose CT image as a reference image [37]. A combination of Non-Local means and TV minimization has been reported in [38]. However, the application of Non-Local prior is limited especially in 3D systems, due to its huge computational cost.

In this paper, we propose a fast iterative reconstruction algorithm for sparse view cone-beam CT. The method is based on the classical maximum a posteriori (MAP) framework with a large-scale Non-Local means prior to constraint optimization. The whole algorithm is carried out under the CUDA parallelization framework for acceleration. In previous work, we have already proposed a fast parallelization of the projection and back-projection operator [39]. Here, we define ordered subsets in the image domain to reduce the huge computational cost of 3D NLM prior. The paper is organized as follows: In "Reconstruction Model" section, we describe the MAP reconstruction model with 3D Non-Local means prior. "Experiments" describes in detail the optimized calculation scheme and the CUDA parallelization. The reconstruction results obtained from simulated data and real acquisitions together with comparisons to other competing methods are given and discussed in "Discussion" section. A conclusion is provided in "Conclusion" section.

Reconstruction model

Given the projection measurements y and an X-ray attenuation function f, according to the Bayesian law, the posterior distribution is:

$$P(f|y) = \frac{P(y|f)P(f)}{P(y)} \tag{1}$$

where $P(f|y)$ is the likelihood function.

The MAP estimator is defined by:

$$f^{MAP} = \arg\max_{f}(P(f|y)) \tag{2}$$

The optimization of (2) can be performed using its logarithm form:

$$f^{MAP} = \arg\max_{f}(L(f) + \beta U(f)) \tag{3}$$

where $L(f) = \log(P(y|f))$ is the log-likelihood and $U(f) = \log(P(f))$ is the prior term, β is hyper-parameter that controls the balance between log-likelihood and prior. The log-likelihood is usually assumed to be independent and obeys a Poisson distribution, but in real cases, it is often approximated by weighted Gaussian distributions with the following definition:

$$L(f) = \sum_{I} (y - \mathbf{A}f)^T D(y - \mathbf{A}f) \tag{4}$$

where $A = \{a_{ij}\}$ is projection operator. The weighting matrix D is a diagonal matrix, its coefficients d_i are proportional to detector counts, which are Maximum Likelihoods estimates of the inverse of the variance of the projection measurements [40]. We use the following definition:

$$d = \frac{1}{\sigma^2_{y_i}} \cong I_i \exp\{-\max(\overline{y_i}, \varepsilon)\} \tag{5}$$

where I_i is the photon intensity, which is assume to be a normalized constant in practice without loss of generality; $\overline{y_i}$ is a smooth version of projection measurements, and ε is a constant to prevent the excessive weighting. The most commonly considered definition of $U(f)$ is the Gibbs prior, with the following form

$$U(f) = \sum_{j} \sum_{k \in W_j} w_{jk} \Phi(f_j - f_k) \tag{6}$$

where W_j represents the neighboring window of pixel x_j; w_{jk} is the weight between $x_k$and x_j, and is inversely proportional

to their Euclidean distance in the image space. The potential functions Φ characterize the interaction inside cliques in neighborhood regions, like Lp norm: $\Phi(t) = \|t\|_p$.

The definition of the prior term is critical to get effective reconstructions. In iterative algorithms aimed at solving highly ill-posed problems, a well-designed prior should prevent the solution from falling into local minimal. A frequently considered choice in sparse view scan reconstruction is the total variation (TV) prior, with the potential function defined as: $\Phi(t) = |\nabla t|$, known as capable of preserving smooth regions and sharp edges.

Non-Local regularization

Although the TV prior has been considered effective in sparse view CT reconstruction, it makes use of low-order neighborhood with small patch size. In other words, only very local information is used as constraint. As the number of projection views decreases, this TV prior does not provide enough constraint for the optimization and streak artifacts appear in the reconstruction.

The idea of Non-Local prior is derived from the Non-Local means filter in image denoising, The Non-Local means filter is a large-scale nonlinear filter based on a relatively wide neighborhood (search window) which considers the similarity between patches (i.e. the similarity patch-window). The full use of the similarity structure in the image space leads to a better performance in denoising and edge-preserving. For Non-Local prior and according to Eq. (6), the weight w_{jk} between pixel x_j and pixel x_k is calculated as follows:

$$w_{jk} = \frac{1}{Z(j)} e^{\frac{-\left\|v(\aleph_j)-v(\aleph_k)\right\|_p}{h^2}} \tag{7}$$

where $\aleph_j$ and $\aleph_k$ are respectively neighborhoods centered on voxel x_i and voxel x_j; $v(\aleph_j)$ and $v(\aleph_k)$ are voxel vectors in $\aleph_j$ and $\aleph_k$; $\|\bullet\|_p$ is the p-norm function (throughout this paper, we choose $p = 1$ because the L2-norm leads to over smoothing effect); h is a parameter controlling the decay of the exponential function and $Z(i)$ is a normalization factor defined as:

$$Z(j) = \sum_k e^{\frac{-\left\|v(\aleph_j)-v(\aleph_k)\right\|_p}{h^2}} \tag{8}$$

The limitation of Non-Local means prior use in cone-beam reconstructions is its excessive computation cost. If we consider the case corresponding to a reconstructed voxel number J, a search window size M and a patch window size N, the computational complexity when using Non-Local prior is O(JMN) while for the conventional Gibbs prior it is O(J). By increasing M and N, the nonlocal prior tends to provide stronger constraint thus generating better reconstructions with effective noise suppression.

For instance and to get a quantitative index, in one of our experiments, for an unknown 3D image set to $512 \times 512 \times 512$, a detector plane resolution 1000×668 and 120 projections, for each view, the projection and back-projection takes about 90.45 s in total, with the parallelized computation method described in [39]. The computation time for Gibbs prior with one order neighborhood takes only 432 ms (also with CUDA parallelization). For the Non-Local prior model with search and patch windows of $21 \times 21 \times 21$ and $7 \times 7 \times 7$ respectively, the computation cost is 1268.32 s, which takes over 93% of the computation time. Thus, the acceleration of Non-Local prior model is the main problem in practice.

Ordered sub-window search

The L-p norm in (7) is a similarity measure between patch windows weighting the constraint provided by different patches. When using a large search window, the patches are redundant, that is to say, for a certain search window, we can still have a similar constraint with fewer patches. This is also the case in the projection step. In [41], the authors introduce the OSEM algorithm and proved the convergence in the condition of subset balance. The OSEM algorithm is based on the idea that the projections are redundant, i.e. adjacent projection views carrying almost the same information. The projection views are separated into n subsets (normally non-overlapping subsets) at each iteration and one subset is chosen for the projection and back-projection steps. Although the OS algorithms are not globally convergent, the reconstruction results are shown to be similar to those using the full projection views, but the computational cost is lowered to $1/n$. This is the reason why the OS algorithms have been widely used in reconstruction [42–45].

Inspired by the OS idea, we can as well separate the search window into subsets. Suppose that the search window size is equal to K^3, the size of the patch window to Q^3, then each search window contains K^3 overlapping patches. Thus, we can generate M subsets, each subset having K^3/M patches. For each voxel, only one subset is involved in the calculation of the prior at each iteration. Such scheme is referred to as the ordered subset search (OSS). Similarly to the ordered subsets in the projection domain, the alternate subsets also lead to varied solutions. In order to prevent the convergence problem, in the proposed method, the patches in each subset are evenly distributed in the search window, with the same sample distance as shown in Fig. 1 in the 2D case.

With this OSS scheme, the computation cost of Non-Local prior is reduced to 1/M when compared to the original

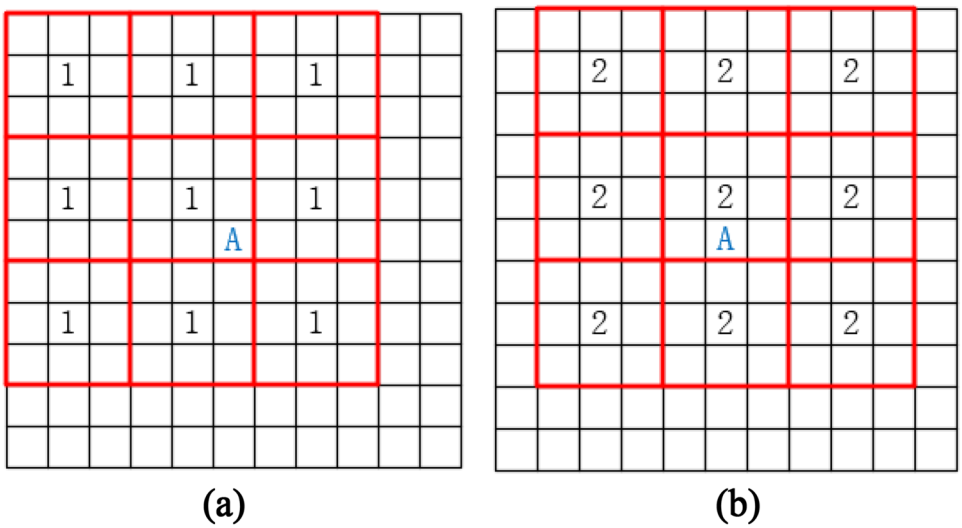

Fig. 1 An example of ordered subsets in a 2D image space. A is current central pixel, the whole grid is the search window for pixel A and each red square is a patch window with size 3×3: **a** is the first subset, **b** is the second subset

implementation. Therefore, we combine in our approach the OS in the projection domain with the OSS in the neighborhood region together. The flowchart of our OSS Non-Local constrained MAP algorithm is summarized in Table 1.

Experiments

The proposed method is evaluated on both simulations and real acquisitions. All experiments are carried out on a computer with CORE i5-2400 CPU and Nvidia GeForce GTX TITAN Black. The programming environment is Microsoft Visual Studio 2012 and CUDA 7.0.

Phantom test

In the phantom test, we use dataset scanned from CATPHAN phantom for reconstruction. The system configuration is as follows: the source-axis distance (SAD) is 1000 mm; the source-imager distance (SID) is 1500.412 mm; the size of detector plane is 1024×768; the detector size is $0.388 \times 0.388\,\text{mm}^2$; the reconstruction object is with size $840 \times 840 \times 420$ and the voxel size is $0.33 \times 0.33 \times 0.33\,\text{mm}^3$. The total number of projection views is 686, uniformly distributed over 2π. In order to evaluate the performance of low contrast area recovering, we perform simulate projection on an irregular star shaped region, shown in yellow box on the left side of Fig. 2. The simulated projection is overlayed to the phantom projections. Reconstructions are performed on both the original and overlayed projections.

We first use full projection view (686 views) sequence for reconstruction. Figure 2 shows the reconstruction results. The window center is 50 and window width is 450. Besides the FDK reconstruction from modality, MAP algorithm with TV prior, proposed OSS Non-Local and conventional Non-Local prior are considered. The size of the search window is set to $21 \times 21 \times 21$ and the size of similarity patch-window is $5 \times 5 \times 5$ for both the OSS and conventional Non-Local prior; the patches are separated into 27 subsets for the proposed OSS Non-Local. The first row shows the results with original projections; the second row shows the results with overlayed projections. The red boxes between two rows are zoomed subtraction regions marked as blue box in Fig. 2e, the yellow box is the original shape of the overlayed object. From Fig. 2 we can see that the noise level in FDK reconstruction is relatively higher than those resulting from iterative methods. The non-local prior provides better edge recovery than the TV prior. The difference between the proposed OSS Non-Local prior and conventional Non-Local prior is very small (the SSIM [46] ratio between the two images is 0.9985).

We then reduced the number of projections to 98, uniformly distributed over 2π. Besides the MAP-TV algorithm, the T_pV minimization method [22] with $p = 0.5$ is also considered for comparison. For the proposed OSS Non-Local prior, the size of the search window is set to $21 \times 21 \times 21$; the size of similarity patch-window is $5 \times 5 \times 5$; the number of subset is set to be 27. For iterative methods, reconstructions are done with different weighting parameters, the results with lowest noise ratio are selected and shown in Fig. 3.

From Fig. 3, we can see that as the number of view decreases, artifacts begin to show up in the FDK reconstructions, and the star shaped low-contrast area is hard to distinguish. For the iterative methods, although the reconstructions have good overall visual appearance, we may see that the subtracted star area is distorted in the MAP-TV reconstruction; it is smoother in the T_pV result, but the angles are not well

Table 1 Flowchart of the proposed OSS Non-Local constrained MAP algorithm

1) Initialize f^0 with zero values;

2) Separate the projection set S into N non-overlapped subsets, each subset is defined as S_n $n \in [1, N]$;

3) For each voxel f_j, the patch set in search window is W_j. Separate the patches into M non-overlapped subsets, each subset is specified as W_j^m, $m \in [1, M]$.

4) Set iteration number t =0 and repeat 5) until the stopping criterion is reached:

5) For each projection set S_n:

a) calculate the projection residual Δ_n:

$$\Delta_n = \frac{y_i}{\tilde{y}_i}, \text{ in which } y_i \in S_n, \ \tilde{y}_i = \sum_j a_{ij} f_j;$$

b) Choose the subset index in image space according to the iteration number: $m = (t\%\mathrm{M}) + 1$;

c) For each voxel f_j

i. calculate the OSS penalty term for voxel j:

$$\frac{\partial U(f)}{\partial f_j} = \sum_{k \in W_j^m} w_{jk} \frac{\partial \Phi(f_j - f_k)}{\partial f_j}$$

ii. Update f_j via:

$$f_j^{t+1} = \frac{f_j^t}{\sum_i a_{ij} + \beta \frac{\partial U(f^t)}{\partial f_j^n}} \sum_i a_{ij} \Delta_i, i \in S_n$$

d) $t = t + 1$

e) Stop iteration when one of the following conditions is true:

i. $t \geq T$

ii. $\left\| f^{k+1} + f^k \right\|_2^2 < \varepsilon$

recovered; the OSS-Non-Local MAP is more robust and provides the best recovery among all the methods above.

To complement the visual quality inspection of the reconstructions provided by the different methods, we use PSNR (Peak Signal to Noise Ratio) and SSIM (structural similarity index): ×being the recovered signal vector and y the reference vector, the PSNR is defined as:

$$PSNR(x, y) = 20 \log_{10} \left(\frac{\max(y)}{\sqrt{MSE}} \right) \quad (9)$$

where MSE is the mean square error defined as:

$$MSE = \|x - y\|_2^2 / M \quad (10)$$

M is the number of voxels/pixels. The SSIM is defined in [46]. Both PSNR and SSIM are calculated for the entire image.

We take Fig. 2d, h as reference images for original and overlayed projection reconstruction respectively. Table 2 shows the PSNR and SSIM values obtained from sparse view reconstructions by the different iterative methods. These results confirm the visual assessment performed above. They point out in particular that the methods based on Non-Local priors lead to better values of PSNR and SSIM than the MAP-TV and T_pV approaches.

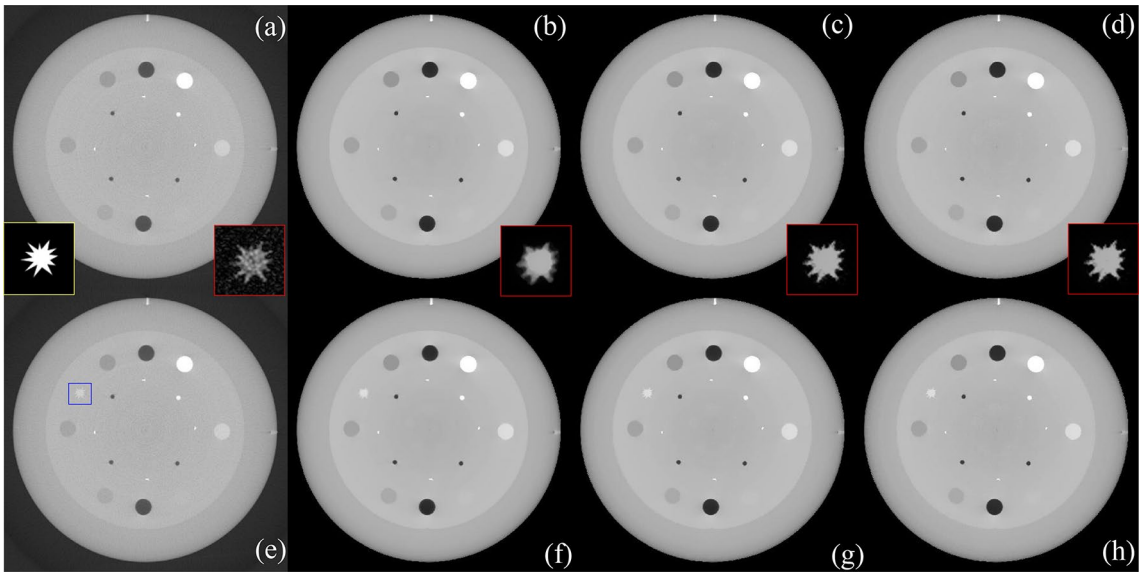

Fig. 2 Reconstruction results from 686 projection views. The first row are results with original projections and the second row are results with overlayed projections: **a**, **e** FDK; **b**, **f** MAP-TV; **c**, **g** OSS Non-Local MAP; **d**, **h** conventional Non-Local MAP. The red boxes show the zoomed subtractions (in blue box)

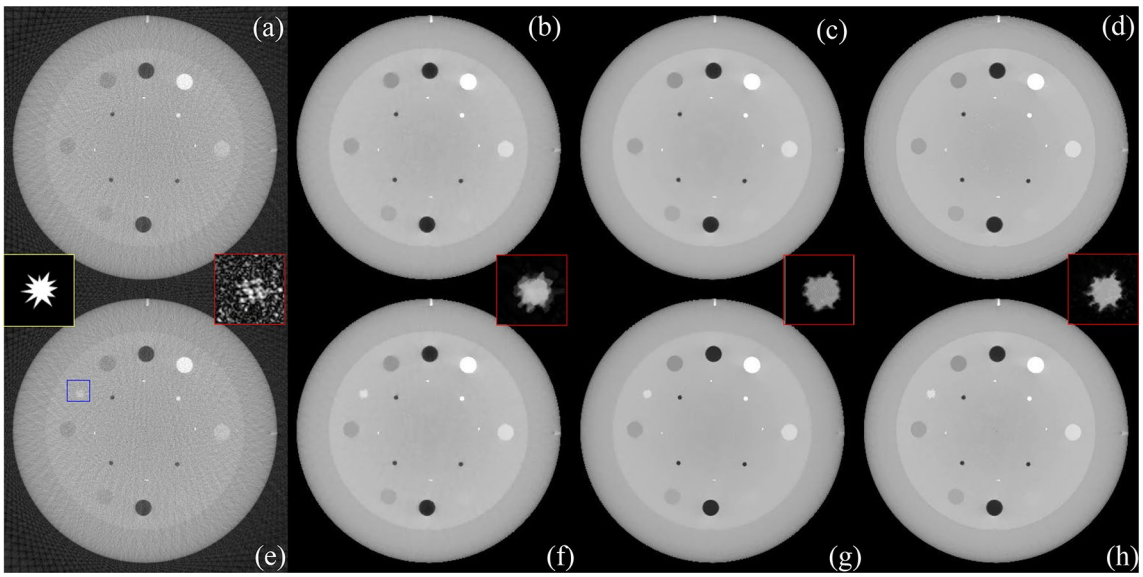

Fig. 3 Reconstruction results from 98 projections views. The first row shows the results obtained with the original projections and the second row the results with overlayed projections: **a**, **e** FDK; **b**, **f** MAP-TV; **c**, **g** T_pV minimization; **d**, **h** OSS Non-Local MAP. The red boxes show the zoomed subtractions (in blue box)

CBCT acquisition

The CBCT (Cone-Beam Computed Tomography) projection images of a human head are collected from Shandong Cancer Hospital and Institute (OBI, Varian Medical Systems), with 650 uniformly sampled projection views. The SAD is equal to 1000 mm and the SID to 1500 mm. The detector plane has 768×1024 pixels with a pixel size of $0.388 \times 0.388\,\text{mm}^2$. The reconstructed volume is defined on a $768 \times 768 \times 384$ grid with a voxel size set to $0.3 \times 0.3 \times 0.3\,\text{mm}^3$.

The OSS Non-Local constrained reconstruction performed using the whole projections sequence serves as the reference. For comparison and to assess the performance of the method, uniformly down-sampled subsets with 130

Table 2 PSNR and SSIM for results in Fig. 4

Algorithm	Original projections		Overlayed projections	
	PSNR	SSIM	PSNR	SSIM
MAP-TV	35.40	0.9461	35.39	0.9460
T_pV	39.58	0.9712	39.57	0.9711
OSS Non-Local	47.93	0.9763	47.91	0.9763

projections are used. In the reconstruction process, we set the size of the search window to $27 \times 27 \times 27$, the size of similarity patch-window to $7 \times 7 \times 7$ and the number of patch subsets to 81.

Figure 4 gives the reconstruction results using 650 projections. For the iterative methods, the window center is 80 and window width is 280; the FDK result is scaled to similar display window. In Fig. 6, both the proposed OSS Non-Local and TV priors provide good reconstructions and very close images (SSIM: 0.9835). The difference between OSS and conventional Non-Local constrained results are even lower (SSIM: 0.9949). The reconstruction obtained through the proposed method is kept as the reference image below.

Figure 5 shows the reconstructions with 130 projections. All the reconstructions are subtracted to the reference image in order to get better insights of the degradations occurring with fewer projections. It can be seen in Fig. 5 that, as the number of projections reduced to 20% of the full scan views, the TV prior is not capable of providing enough constraint and therefore piecewise blocked artifacts appear. Such artifacts can be successfully suppressed with the T_pV minimization. The proposed OSS Non-Local-L1 prior still works will and provide smoother piecewise region recovery and shaper edges. Table 3 provides the PSNR and SSIM values under 130 projection views, to confirm the qualitative results described above.

Micro-CT acquisition

The same experimental process is applied to Micro-CT scan (Modality: SkyScan 1176) data of a rat. Compared to CBCT, the gray level resolution of Micro-CT is low but the edges are sharp and clear. The configuration of the Micro-CT is as follows: the SAD is 120.6 mm; the SID is 171.1 mm; the total projection number is 1200; the size of these projection images is 668×1000 with pixel size $0.0504 \times 0.0504\ \text{mm}^2$. The size of the reconstructed volume is $840 \times 840 \times 420$ and the voxel size is $0.035 \times 0.035 \times 0.035\ \text{mm}^3$.

Here also, the OSS Non-Local means based reconstruction using the full projection sequence is taken as reference. To evaluate the performance of the proposed method, comparisons are carried out with 120 projections. The size of search window is $27 \times 27 \times 27$ with a number of patch-subsets equals to 81 while the size of the similarity patch-window is $5 \times 5 \times 5$.

Figure 6 highlights the reconstructions performed with 1200 projections. The window center is 90 and window width is 240. Ring artifacts can be observed in Fig. 6a because a consistency correction should be done for each projection before reconstruction. However, we do not have access to the synchronous collected blank scan, and as a result, the response of each detector line is not perfectly

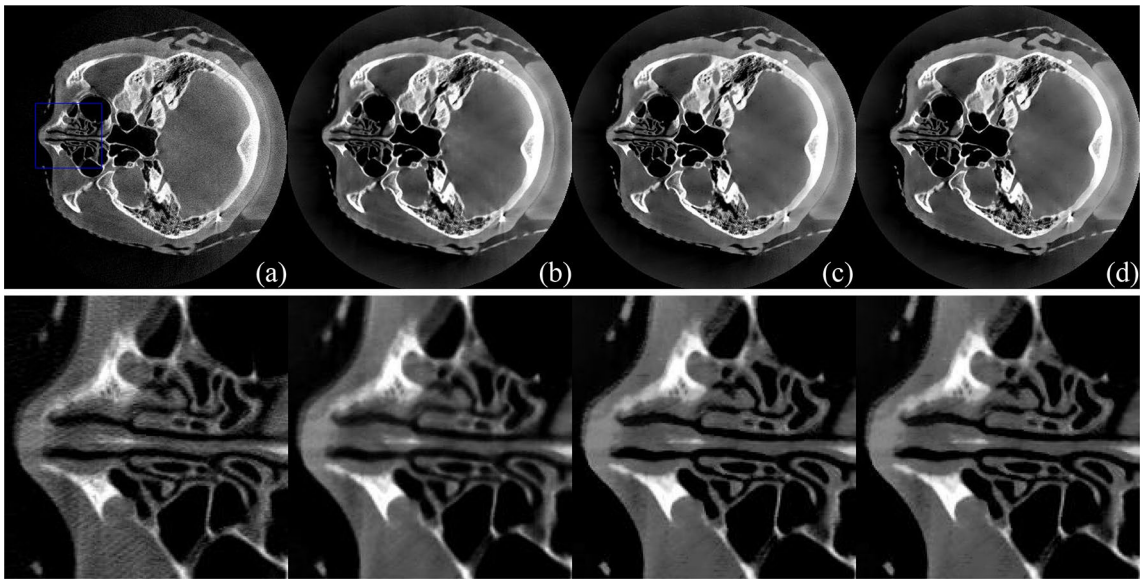

Fig. 4 Reconstructions results with 650 projection views, with **a** FDK; **b** MAP-TV; **c** OSS Non-Local MAP; **d** conventional Non-Local MAP. Their corresponding zoomed ROIs (defined by the blue box) are displayed in **e** and **h**

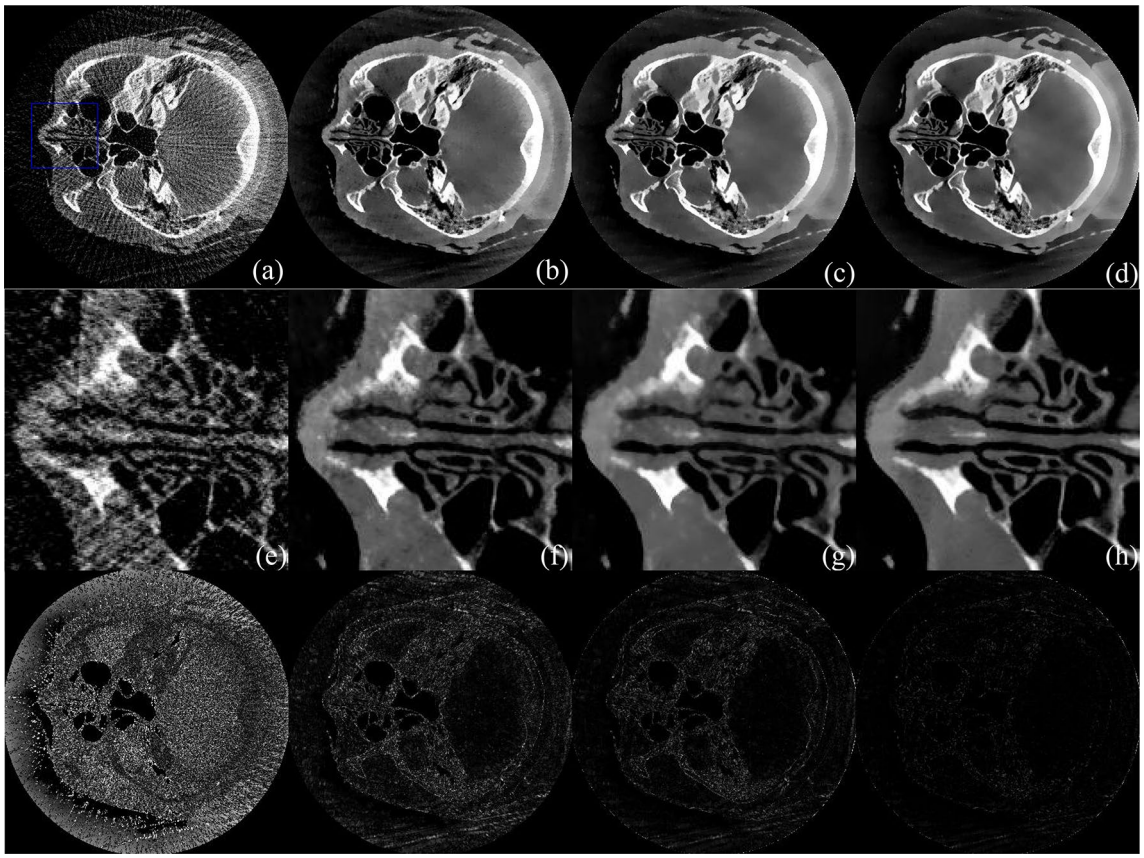

Fig. 5 Reconstruction results with 130 projection views: the first row displays the reconstructions with: **a** FDK, **b** MAP-TV, **c** T_pV, **d** OSS Non-Local prior; the second row displays the respective zoomed ROIs (indicated in the blue box); the third row depicts the corresponding subtracted images according to the reference in Fig. 4d

Table 3 PSNR and SSIM of results in Fig. 6

Algorithm	130 angles	
	PSNR	SSIM
MAP-TV	37.32	0.8681
T_pV	42.78	0.9186
OSS Non-Local	45.33	0.9429

aligned. In Fig. 8b–d, the priors allow suppressing these ring artifacts. As seen in the previous experiment, the TV prior, OSS Non-Local prior and conventional Non-Local provides similar results with full view scan. The SSIM between TV an OSS Nonlocal is 0.9821; the difference between OSS and conventional Non-Local is 0.9958. For all the three iterative methods, a good performance in artifact removal and boundary preserving can be observed. We take the OSS Non-Local result as reference for evaluation.

Figure 7 shows the evolution of the reconstructions when decreasing the number of projections with 120 projections. In Fig. 7b, the artifacts are not fully suppressed while they are cancelled with T_pV and OSS Non-Local MAP. Similar to the experiment above, the T_pV effectively suppresses the noise thus provide smooth reconstructions, but the small low contrast targets inside the lung cannot be observed in Fig. 7g. The OSS Non-Local again shows the best performance among the three iterative methods.

The PSNR and SSIM values reported in Table 4, confirm that the proposed method performs well in very sparse view reconstruction (here also Fig. 8c is used as the reference image).

Computation time

Table 5 shows the computation time for Non-Local prior. The acceleration ratios are around 27 for the phantom test and around 81 for the head cone-beam scan and Micro-CT scan, which are in accordance with our expectations (the number of subsets involved). We change the number of subsets to 27 and 243 respectively and perform the reconstruction using the Micro-CT scan data. The reconstructions using these different subset settings are shown in Fig. 8 and they look very similar; the subtractions to Fig. 8c are also close to each other. Taking Fig. 6c

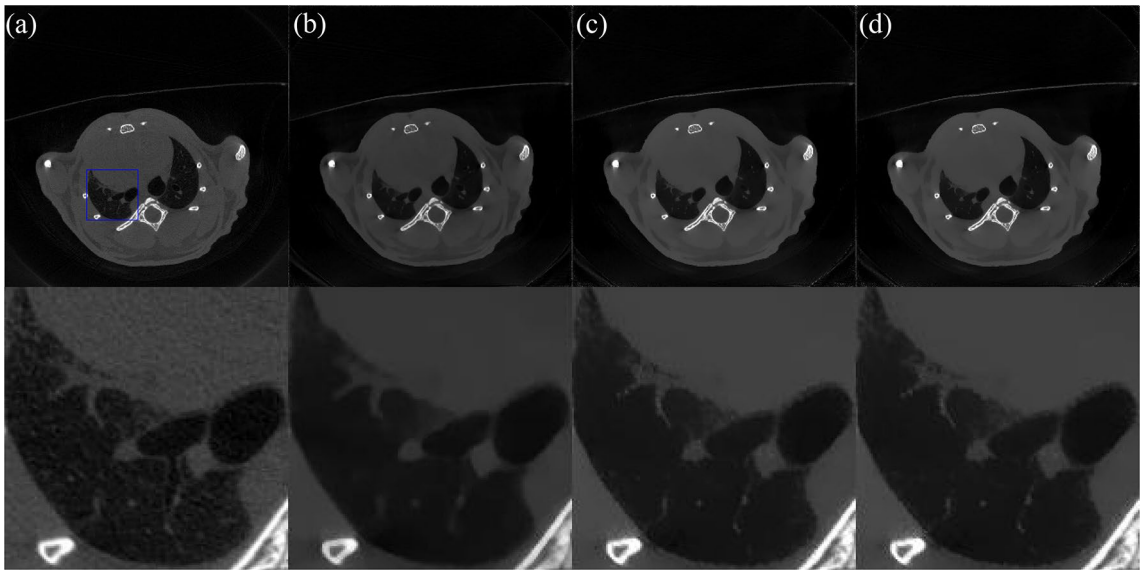

Fig. 6 Reconstruction results with 1200 projections views: **a** FDK; **b** MAP-TV; **c** OSS Non-Local MAP; **d** conventional Non-Local MAP. **e**–**h** are the zoomed ROIs (specified by the blue box) in **a**–**d**

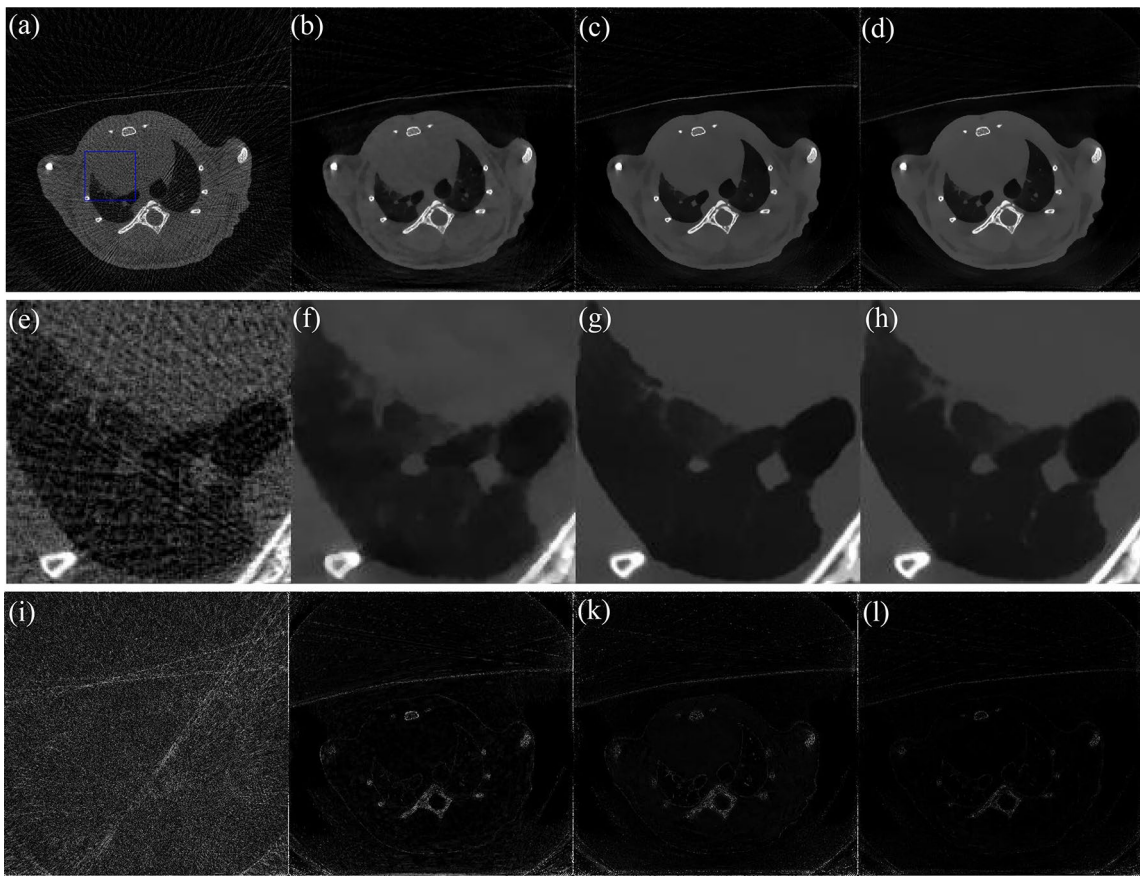

Fig. 7 Reconstruction results with 120 projections views: **a** FDK; **b** MAP-TV; **c** T_pV; **d** OSS Non-Local MAP. **e**–**h** display the zoomed ROIs (in blue box). **i**–**l** are the subtraction of these images with the image in Fig. 6d

Table 4 PSNR and SSIM of results in Fig. 8

Algorithm	120 angles	
	PSNR	SSIM
MAP-TV	36.87	0.8998
T_pV	43.22	0.9339
OSS Non-Local	46.03	0.9457

Table 5 Computation times (in seconds) for the above experiments

Dataset	Non-Local (s)	OSS Non-Local (s)
Phantom tsest	1002.2	40.2
CBCT	1695.1	20.8
Micro-CT	2249.0	27.6

Table 6 Computation times when varying the number of subsets for the Micro-CT scan (in seconds)

Number of subsets	OSS Non-Local (s)
27	80.5
81	27.6
729	3.09

as reference, the PSNR of the three reconstructions are respectively 46.34, 46.03 and 45.68 from left to right. So, using fewer patches in each dataset does not degrade the overall image quality. But the noise suppression ability is slightly weakened according to the PSNR because the more subsets we use, the less patches contained in one subset. The computation costs shown in Table 6 indicate that the acceleration will increase with the number of subsets used.

Discussion

There is a consensus in using high-dose FBP reconstruction as reference for low-dose CT denoising method assessment [47]. This is the case for instance in dictionary training and sample labelling based on deep learning [48, 49]. However in our case, the X-ray images are sheltered by objects such as the scan bed out of the FOV reconstruction. The X-ray attenuation in these objects leads raised background value in FDK reconstructions. Besides, the lack of blank scan results in ring artifacts in the FDK reconstructions. Thus, we choose to use Non-Local constrained reconstructions with full view scan as reference image to evaluate the performance of sparse view scan in the three experiments above. Although

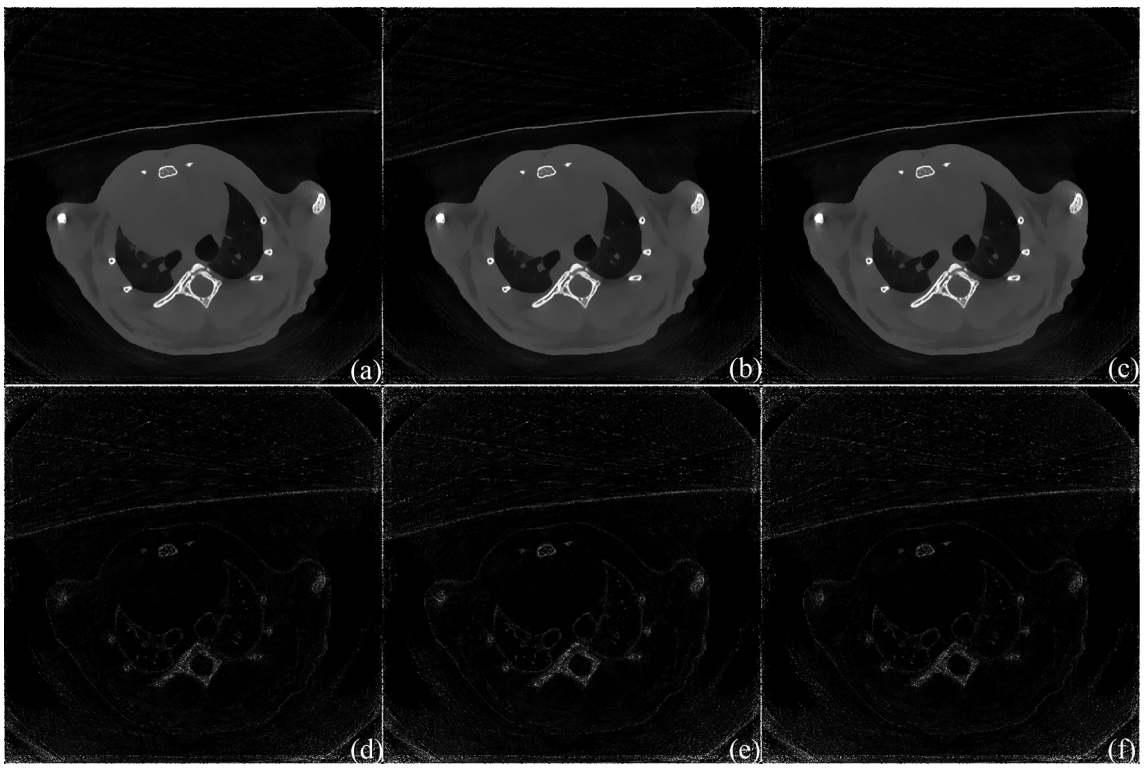

Fig. 8 Reconstructions performed using 120 Micro-CT views with: **a** 27 subsets; **b** 81 subsets; **c** 243 subsets; the second row shows the corresponding subtracted images using the reference in **c**

using Non-Local reconstructions as reference may lead to bias toward Non-Local means based sparse view reconstruction, the first experiment demonstrates that the Non-Local constrained results better matches the ground truth. In the sparse view reconstructions, the T_pV shows excellent performance in providing smooth reconstructions, yet the proposed method seems to be superior in recovering detail features, such as low contrast area and small sharp angles.

Instead of introducing adaptive parameter decision scheme, all the results are chosen from the best results obtained via manually selected parameters. For the proposed method, besides subset count, there are four parameters to set before iteration: size of search window, size of patch window, weighting parameter, as β in (3), and variance parameter, as h in (7). Theoretically, large search window and large patch window should lead to better results, yet we should notice that on the one hand, the size of search window and patch window are direct proportion to the computation cost; on the other hand, a large patch window is not always benefit to the reconstructions, especially for complex area with irregular texture. In this paper, we the search window size is between $21 \times 21 \times 21$ to $27 \times 27 \times 27$, the patch window size is $5 \times 5 \times 5$ or $7 \times 7 \times 7$. We have tried with larger window sizes, but the results varies slightly. The weighting parameter β controls the balance between projection fidelity and prior penalty, large β brings over-smoothed reconstructions, while too small β fails to provide enough control to the noise and artifacts. The variance parameter controls the convexity of the potential function. Generally speaking, small h tend to provide strong edge preserving ability, but accompanied with higher probability of divergence; large h is more likely to offer over-smoothed result. The parameter h has to be chosen according to the variance of scanned target, for example, use a small h for target with small variation so as to get piecewise smooth reconstructions; use a large h for target with large variation so as to prevent divergence. Self-adaptive scheme on the variance parameter based on local variance in small patches will be discussed in future work.

Conclusion

In this paper, we propose an approach exploiting a Non-Local means prior model for iterative cone-beam CT reconstruction. It relies on an ordered subset search for the computation of the prior term. For each voxel, the search window is divided into non-overlapping subsets, each of them containing a number of patch windows. The subsets are then use alternatively over iterations. The experiments conducted on CBCT and Micro CT scans show that, when compared to the TV prior, the Non-Local means prior provides much better reconstructions in real sparse-view scans. Although the computational cost of this prior is high, the proposed OSS scheme leads to significantly reducing this cost while preserving the reconstruction quality.

Acknowledgements The authors are indebted to Dr. Jean-Louis Coatrieux, University of Rennes 1, Inserm U1099, Rennes, France, for his contributions in conducting this work. They thank Prof. Jianhua Ma from Southern Medical University, Guangzhou, China, for providing the experimental data. They also thank Prof. Jinglu Zhang from Nanjing Medical University, Nanjing, China, for her assistance in completing the experiments. This project has been supported by the National Natural Science Foundation of China under Grant No. 81530060; Basic Research Program of Jiangsu Province under Grant (BK20180670); Open Project from Jiangsu Key Laboratory of Oral Diseases, Nanjing Medical University (JSKLOD-KF-1701, JSKLOD-KF-1708); Open Project from Key Laboratory of Computer Network and Information Integration (Southeast University), Ministry of Education, China (K93-9–2014-10C); Science and Technology Plan of Nanjing (201715017).

Compliance with ethical standards

Conflict of interest No conflict of interest exits in the submission of this manuscript, and manuscript is approved by all authors for publication.

Ethical approval All applicable international, national, and institutional guidelines for the care and use of animals were followed.

References

1. Rothenberg LN, Pentlow KS (1992) Radiation dose in CT. RadioGraphics 12:1225–1243
2. Diederich S, Windmann R et al (1999) Pulmonary nodules: experimental and clinical studies at low-dose CT. Radiology 213:289–298
3. Brenner DJ, Hall EJ (2007) Computed tomography—an increasing source of radiation exposure. N Engl J Med 357(22):2277–2284
4. Mannudeep K, Michael MM et al (2004) Strategies for CT radiation dose optimization. Radiology 230:619–628
5. Jung K, Lee K, Kim S, Kim T, Pyeun Y, Lee J (2000) Low-dose, volumetric helical CT: image quality, radiation dose, and usefulness for evaluation of bronchiectasis. Invest Radiol 35:557–563
6. Hyvönen N, Kalke M, Lassas M, Setälä H, Siltanen S (2010) Three-dimensional dental X-ray imaging by combination of panoramic and projection data. Inverse Probl Imaging 4:257–271
7. Mueller J, Siltanen S (2012) Linear and nonlinear inverse problems with practical applications, computational science and engineering, vol 10. SIAM, Philadelphia
8. Donoho D (2006) Compressed sensing. IEEE Trans Inf Theory 52(4):1289–1306
9. E Sidky, P Xiaochuan (2006) Accurate image reconstruction in circular cone-beam computed tomography by total variation minimization: a preliminary investigation. In: Nuclear science symposium conference record, IEEE, vol. 5, IEEE
10. Lustig M, Donoho D, Pauly JM (2007) Sparse MRI: the application of compressed sensing for rapid MR imaging. Magn Reson Med 58(6):1182–1195
11. Trzasko J, Manduca A, Borisch E (2009) Highly undersampled magnetic resonance image reconstruction via homotopic ell-0-minimization. IEEE Trans Med Imaging 28(1):106–121
12. Lu YJ, Zhang XQ, Douraghy A, Stout D, Tian J, Chan TF, Chatzioannou AF (2009) Source reconstruction for spectrally-resolved

bioluminescence tomography with sparse a prior information. Opt Express 17(10):8062–8080
13. Fang LY, Li ST, McNabb RP, Nie Q, Kuo AN, Toth CA, Izatt JA, Farsiu S (2013) Fast acquisition and reconstruction of optical coherence tomography images via sparse representation. IEEE Trans Med Imaging 32(11):2034–2049
14. Yu HY, Wang G (2010) A soft-threshold filtering approach for reconstruction from a limited number of projections. Phys Med Biol 55(13):3905–3916
15. Sidky EY, Kao CM, Pan X (2006) Accurate image reconstruction from few-views and limited-angle data in divergent-beam CT. J X-Ray Sci Technol 14(2):119–139
16. Sidky EY, Pan X (2008) Image reconstruction in circular cone-beam computed tomography by constrained, total-variation minimization. Phys Med Biol 53(17):4777
17. Niu S, Gao Y, Bian Z et al (2014) Sparse-view x-ray CT reconstruction via total generalized variation regularization. Phys Med Biol 59(12):2997
18. Yu HY, Wang G (2009) Compressed sensing based interior tomography. Phys Med Biol 54(9):2791–2805
19. Bian J et al (2010) Evaluation of sparse-view reconstruction from flat-panel-detector cone-beam CT. Phys Med Biol 55(22):6575
20. Han X et al (2010) Algorithm-enabled low-dose micro-CT imaging. IEEE Trans Med Imaging 30(3):606–620
21. Bian J et al (2012) Optimization-based image reconstruction from sparse-view data in offset-detector CBCT. Phys Med Biol 58(2):205
22. Sidky EY, Chartrand R, Boone JM et al (2014) Constrained T_pV minimization for enhanced exploitation of gradient sparsity: application to CT image reconstruction. IEEE J Transl Eng Health Med 2:1–18
23. Chen Z, Jin X, Li L et al (2013) A limited-angle CT reconstruction method based on anisotropic TV minimization. Phys Med Biol 58(7):2119
24. Chen GH, Tang J, Leng S (2008) Prior image constrained compressed sensing (PICCS): a method to accurately reconstruction dynamic CT image from highly undersampled projection data sets. Med Phys 35(2):660–663
25. Lauzier PT, Tang J, Chen GH (2012) Prior image constrained compressed sensing: implementation and performance evaluation. Med Phys 39(1):66–80
26. Candes EJ, Romberg JK (2005) Signal recovery from random projections. Comput Imaging 3:76–86
27. Guo WH, Yin WT (2012) Edge guided reconstruction for compressive imaging. SIAM J Imaging Sci 5(3):809–834
28. Lee JMK, Bresler Y, Ye JC (2011) Compressive diffuse optical tomography: noniterative exact reconstruction using joint sparsity. IEEE Trans Med Imaging 30(5):1129–1142
29. Hu Y, Xie L, Luo L, Nunes JC, Toumoulin C (2011) L0 constrained sparse reconstruction for multi-slice helical CT reconstruction. Phys Med Biol 56(4):1173–1189
30. Zhang JF, Chen Y et al (2015) Gamma prior based reconstruction for low dose CT. Phys Med Biol 60(17):6901–6921
31. Zhang J, Hu Y, Yang J et al (2017) Sparse-view X-ray CT reconstruction with Gamma regularization. Neurocomputing 230:251–269
32. Chen Y, Yang Z, Hu Y, Yang G, Zhu Y, Li Y et al (2012) Thoracic low-dose CT image processing using an artifact suppressed large-scale nonlocal means. Phys Med Biol 57(9):2667–2688
33. Hu Y, Xie L, Meng J, Yang J, Zhang L, Yang B, Chen Y, Luo L, Yin X (2015) Low-dose lung CT processing using weighted intensity averaging over large-scale neighborhoods. Australas Phys Eng Sci Med 38(2):345–356
34. Li Z, Yu L, Trzasko JD, Lake DS, Blezek DJ, Fletcher JG et al (2014) Adaptive nonlocal means filtering based on local noise level for CT denoising. Med Phys 41(1):011908
35. Zhang H, Ma J, Wang J, Liu Y, Lu H, Liang Z (2014) Statistical iterative reconstruction for low-dose CT using nonlocal means-based prior. Comput Med Imaging Graph 38(6):423–435
36. Hang H, Ma J, Wang J, Liu Y, Han H, Lu H, Moore W, Liang Z (2015) Statistical image reconstruction for low-dose CT using nonlocal means-based prior Part II: an adaptive approach. Comput Med Imaging Graph 43:26–35
37. Li B, Lyu Q, Ma J, Wang J (2016) Iterative reconstruction for CT perfusion with a prior-image induced hybrid nonlocal means regularization. Med Phys 43(4):1688
38. Kim H, Chen J, Wang A et al (2016) Non-local total-variation (NLTV) minimization combined with reweighted L1-norm for compressed sensing CT reconstruction. Phys Med Biol 61(18):6878
39. Xie L, Hu Y, Yan B et al (2015) An effective CUDA parallelization of projection in iterative tomography reconstruction. PLoS ONE 10(11):e0142184
40. Thibault JB, Sauer KD, Bouman CA et al (2007) A three-dimensional statistical approach to improved image quality for multislice helical CT. Med Phys 34(11):4526–4544
41. Hudson HM, Larkin RS (1994) Accelerated image reconstruction using ordered subsets of projection data. IEEE Trans Med Imaging 13(4):601–609
42. Kamphuis C, Beekman FJ (1998) Accelerated iterative transmission CT reconstruction using an ordered subsets convex algorithm. IEEE Trans Med Imaging 17(6):1101–1105
43. Erdogan H, Fessler JA (1999) Ordered subsets algorithms for transmission tomography. Phys Med Biol 44(11):2835
44. Kim D, Pal D, Thibault JB et al (2013) Accelerating ordered subsets image reconstruction for X-ray CT using spatially nonuniform optimization transfer. IEEE Trans Med Imaging 32(11):1965–1978
45. Kim D, Ramani S, Fessler JA (2015) Combining ordered subsets and momentum for accelerated X-ray CT image reconstruction. IEEE Trans Med Imaging 34(1):167–178
46. Wang Z, Bovik AC, Sheikh HR et al (2004) Image quality assessment: from error visibility to structural similarity. IEEE Trans Image Process 13(4):600–612
47. Hu Y, Xie L, Meng J et al (2015) Low-dose lung CT processing using weighted intensity averaging over large-scale neighborhoods. Australas Phys Eng Sci Med 38(2):345–356
48. Chen Y, Shi L, Feng Q et al (2014) Artifact suppressed dictionary learning for low-dose CT image processing. IEEE Trans Med Imaging 33(12):2271–2292
49. Chen H, Zhang Y, Kalra MK et al (2017) Low-dose CT with a residual encoder-decoder convolutional neural network. IEEE Trans Med Imaging 36(12):2524–2535